A high-performance dysprosium single-ion magnet with local pseudo cubic geometry

Yanbo Shi,[a] Chennan Zhang,[a] Mingyue Shi,[a] Yang Zhou,[a] Hong Li,[a] Rui Liu,[a] Shaojun Zheng,[a] Aihua Yuan,[a] Lei Chen,*[a] Shu-Yang Chen,*[b] Bing Yin*[c] and Zhao-Bo Hu*[d]

[a]*School of Environmental and Chemical Engineering, Jiangsu University of Science and Technology, Zhenjiang 212003, P. R. China.*
[b]*College of Chemistry and Pharmaceutical Engineering, Nanyang Normal University, Nanyang 473061, P. R. China.*
[c]*Lab of Theoretical Molecular Magnetism, College of Chemistry and Materials Science, Northwest University, Xi'an 710127, P. R. China.*
[d]*Chaotic Matter Science Research Center, Department of Materials, Metallurgy and Chemistry, Jiangxi University of Science and Technology, Ganzhou 341000, P. R. China.*

Electronic Supplementary Information

Table of Contents

Table S1. Crystal data and structure refinements for **1-Dy** and **2-Tb**.

	1-Dy	**2-Tb**
Empirical formula	$C_{80}H_{92}BCl_4N_6O_2Dy$	$C_{80}H_{92}BCl_4N_6O_2Tb$
CCDC no	2351771	2351772
Formula weight	1484.70	1481.12
Temperature / K	193(2)	150(2)
Wavelength / Å	0.71073	0.71073
crystal system	Triclinic	Triclinic
Space group	*P*-1	*P*-1
a / Å	9.9295(4)	9.9470(8)
b / Å	14.2983(7)	14.3125(13)
c / Å	27.6118(13)	27.621(2)
α / deg	78.0990(10)	78.066(3)
β / deg	84.6250(10)	84.619(3)
γ / deg	86.4100(10)	86.448(3)
V / Å^3	3815.3(3)	3826.7(6)
Z	2	2
Z_{calc}, mg/m^3	1.292	1.285
μ / mm^{-1}	1.168	1.112
F (000)	1538	1536
Goodness-of-fit on F^2	1.096	1.083
Final *R* indices [$I > 2\sigma(I)$][a]	R_1 = 0.0522, wR_2 = 0.1214	*R1* = 0.0516, wR_2 = 0.1304
R indices (all data)[a]	R_1 = 0.0600, wR_2 = 0.1258	*R1* = 0.0601, wR_2 = 0.1381

[a] $wR_2 = [\Sigma[w(F_o^2-F_c^2)^2]/\Sigma[w(Fo^2)^2]]^{1/2}$, $R_1 = \Sigma||F_o|-|F_c||/\Sigma|F_o|$.

Table S2. Selected bond lengths [Å] and angles [°] for **1-Dy** and **2-Tb**.

		1-Dy	
Dy1−O1	2.188(3)	O1−Dy1−O1A	180.0
Dy1−N1	2.588(4)	N1−Dy1−N1A	180.0
Dy1−N2	2.609(4)	N2−Dy1−N2A	180.0
Dy1−N3	2.602(4)	N3−Dy1−N3A	180.00(16)
Dy2−O2	2.192(3)	O2−Dy2−O2A	180.0
Dy2−N4	2.569(4)	N4−Dy2−N4A	180.0
Dy2−N5	2.602(4)	N5−Dy2−N5A	180.0
Dy2−N6	2.602(4)	N6−Dy2−N6A	180.0
		2-Tb	
Tb1−O1	2.201(3)	O1−Tb1−O1A	180.0
Tb1−N1	2.609(4)	N1−Tb1−N1A	180.0
Tb1−N2	2.609(4)	N2−Tb1−N2 A	180.0
Tb1−N3	2.597(4)	N3−Tb1−N3A	180.00(15)
Tb2−O2	2.207(3)	O2−Tb2−O2A	180.0
Tb2−N4	2.613(4)	N4−Tb2−N4A	180.0
Tb2−N5	2.617(4)	N5−Tb2−N5A	180.00(10)
Tb2−N6	2.575(4)	N6−Tb2−N6 A	180.0

Table S3. Continuous shape measure (CSM) analyses of eight-coordinate geometries for **1-Dy** and **2-Tb** by SHAPE software.

Eight-coordination	**1-Dy**		**2-Tb**	
	Dy1	Dy2	Tb1	Tb2
Octagon (D_{8h})	33.669	33.919	33.758	33.975
Heptagonal pyramid (C_{7v})	26.136	26.291	26.116	26.323
Hexagonal bipyramid (D_{6h})	6.336	6.391	6.135	6.285
Cube (O_h)	**1.017**	**1.017**	**1.042**	**0.986**
Square antiprism (D_{4d})	11.783	11.817	11.835	11.786
Triangular dodecahedron (D_{2d})	8.793	8.799	8.813	8.772
Biaugmented trigonal prism (C_{2v})	12.851	12.840	12.850	12.836

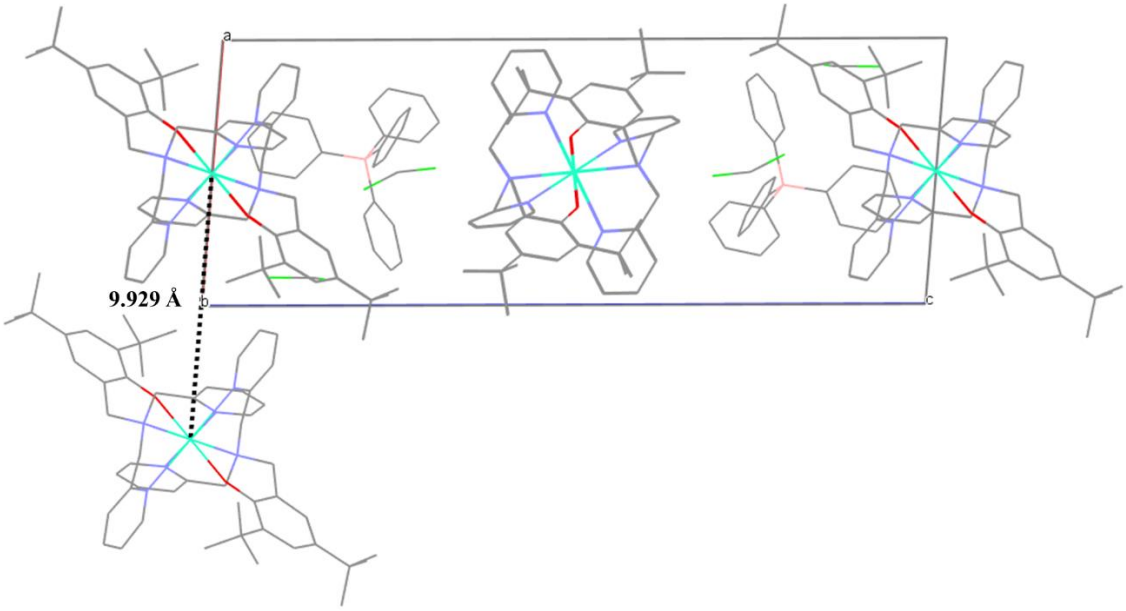

Figure S1. The shortest Dy···Dy distance between adjacent molecules in **1-Dy**. H atoms are omitted for clarity.

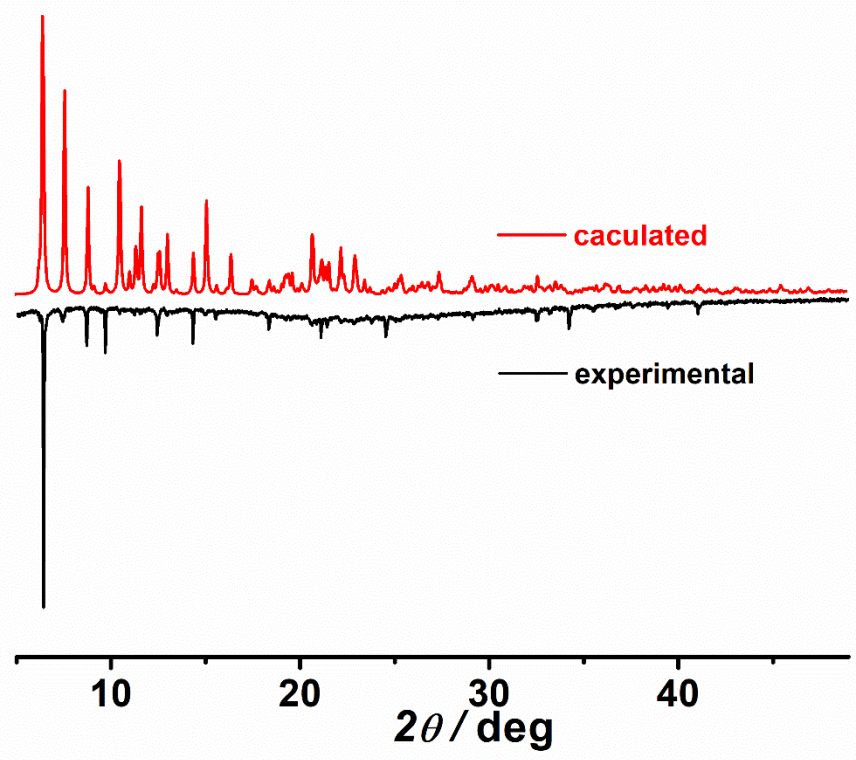

Figure S2. PXRD pattern for complex **1-Dy**.

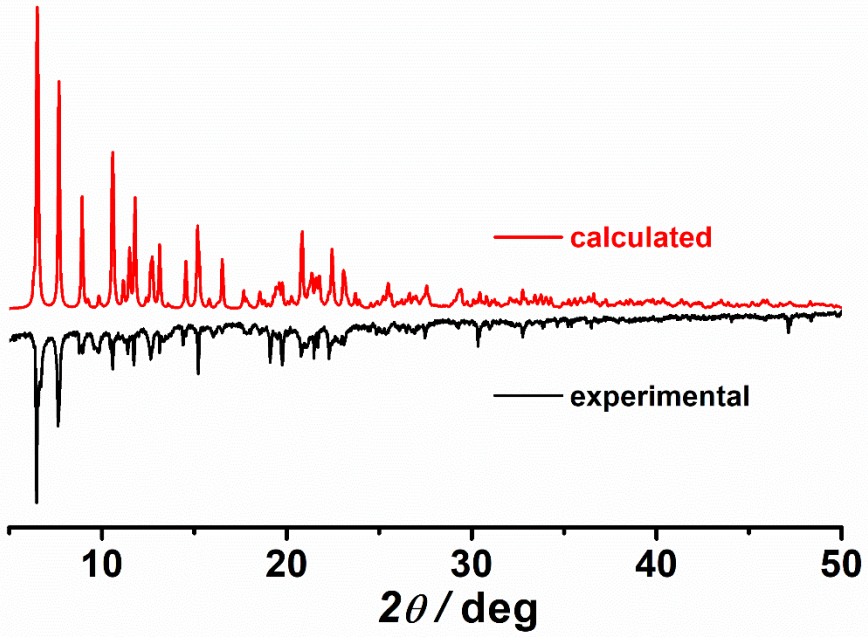

Figure S3. PXRD pattern for complex **2-Tb**.

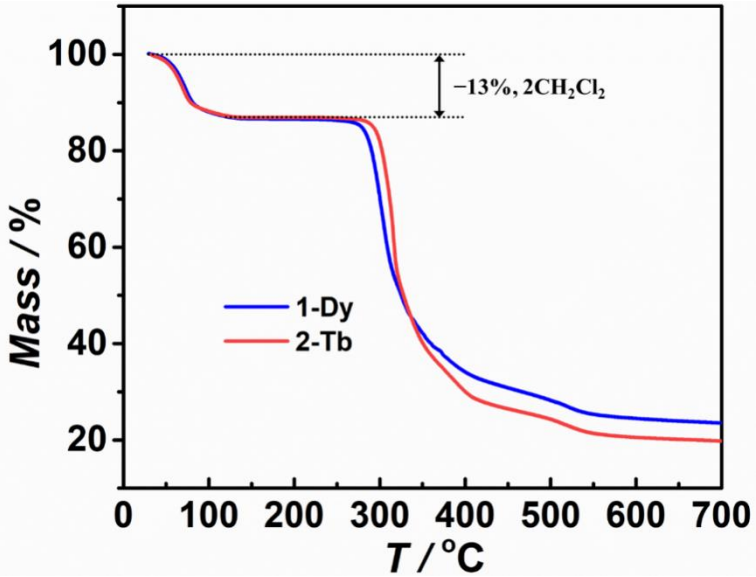

Figure S4. Thermogravimetric analyses of **1-Dy** and **2-Tb**. The black dashed lines show the stage associated with the release of solvent molecules.

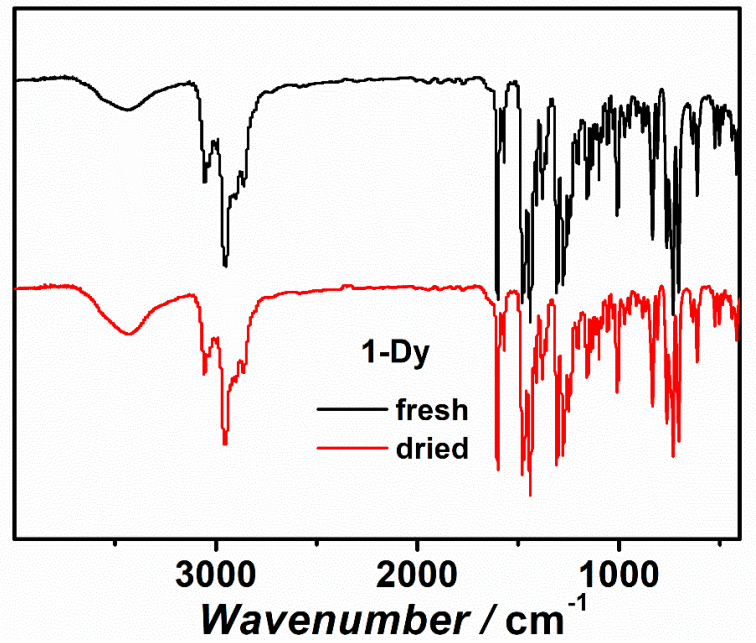

Figure S5. IR spectra for complex **1-Dy**.

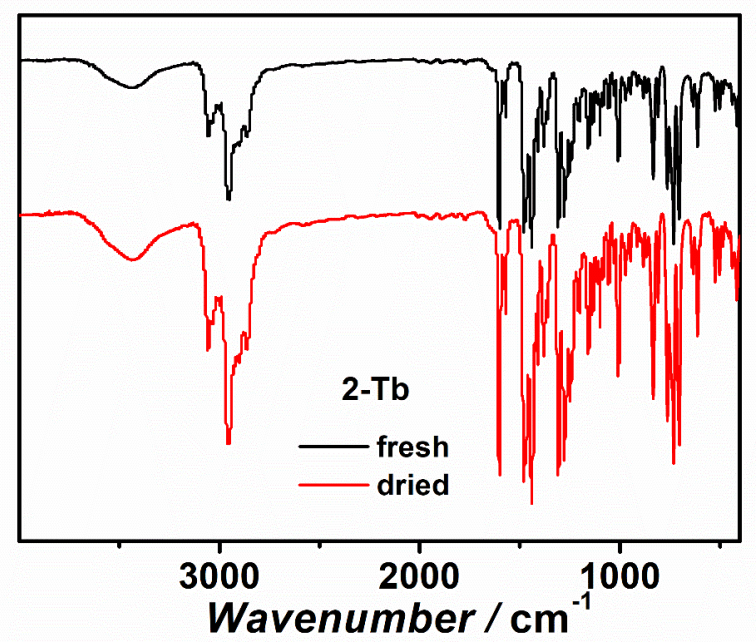

Figure S6. IR spectra for complex **2-Tb**.

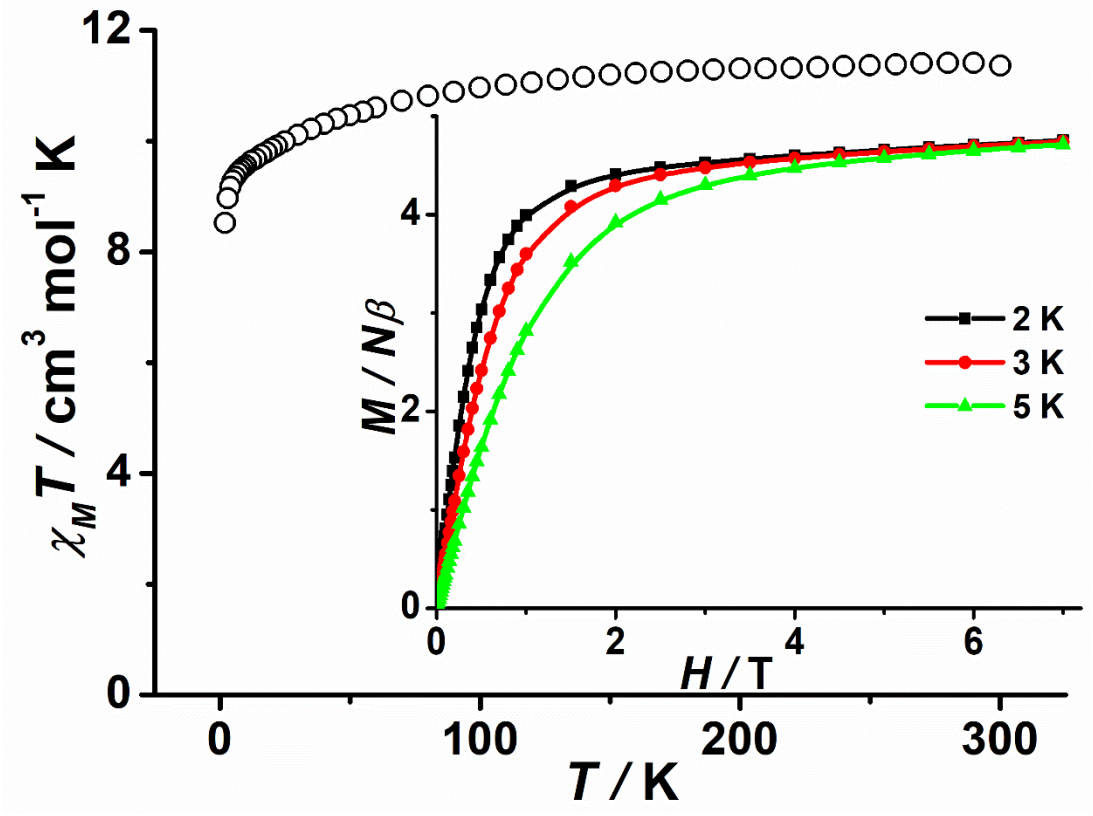

Figure S7. Variable-temperature dc susceptibility data for **2-Tb** in a 1 kOe applied dc field. Inset: Field-dependence of magnetization at 2, 3 and 5 K for **2-Tb**. The solid lines are for eye guidance.

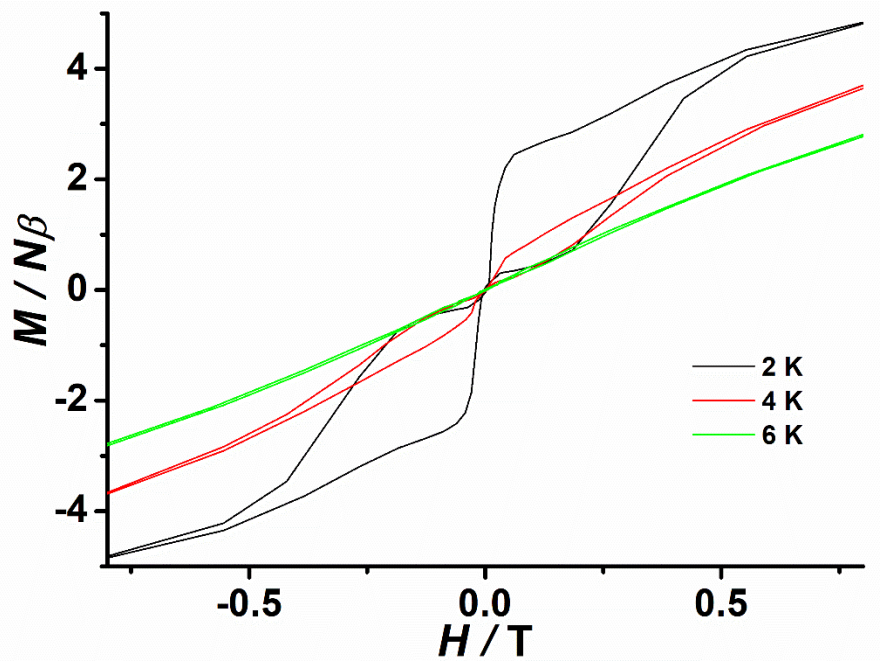

Figure S8. Powder magnetic hysteresis data for **1-Dy** at an average sweep rate of 30 Oe s^{-1}.

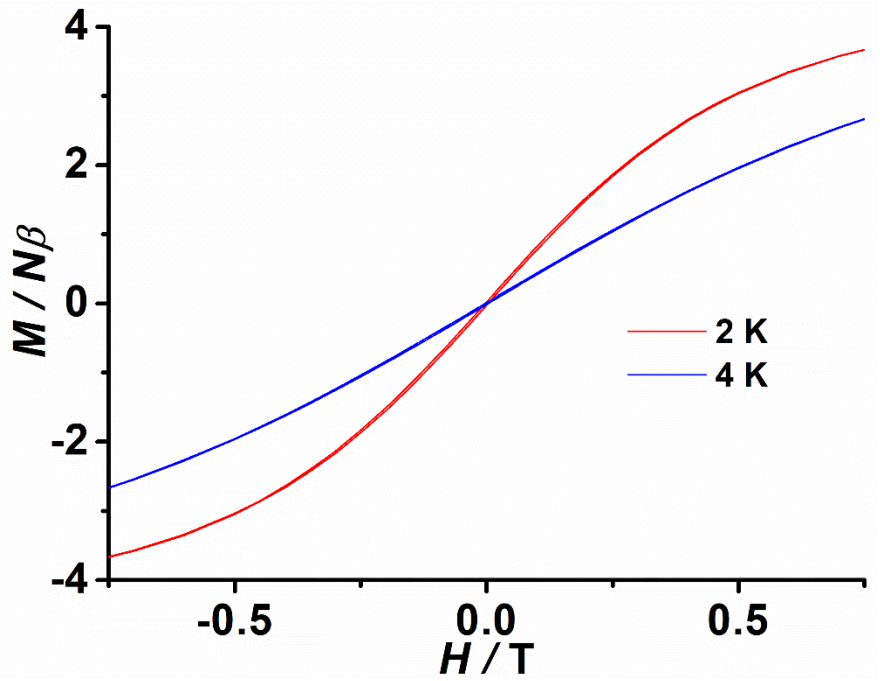

Figure S9. Powder magnetic hysteresis data for **2-Tb** at an average sweep rate of 200 Oe s^{-1}.

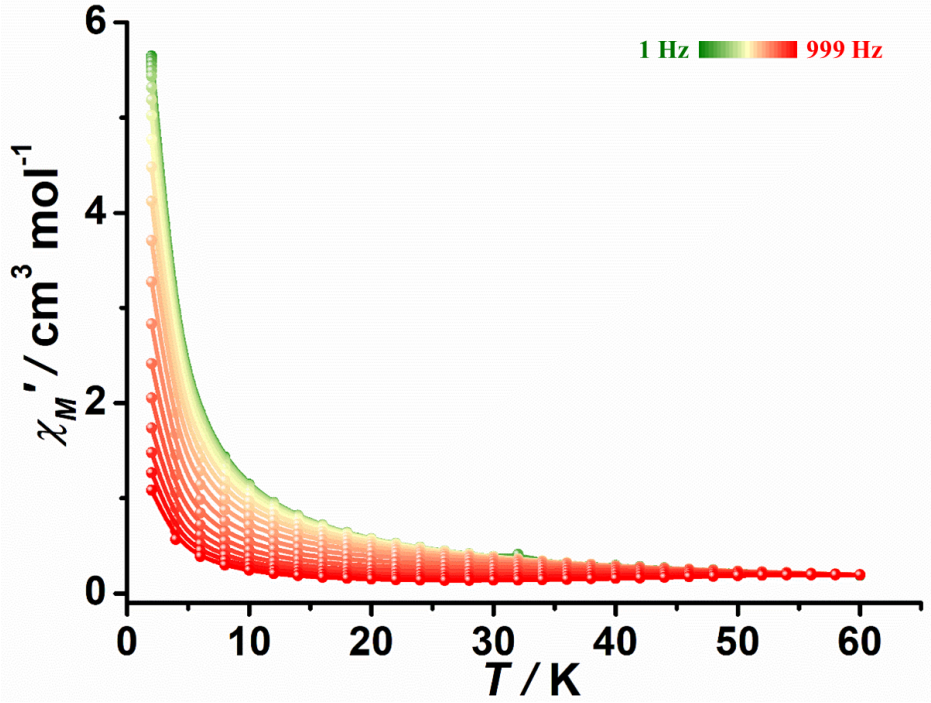

Figure S10. Temperature dependence of in-phase (χ_M') ac susceptibility for **1-Dy** under 0 Oe dc field; the solid lines are guides for the eye.

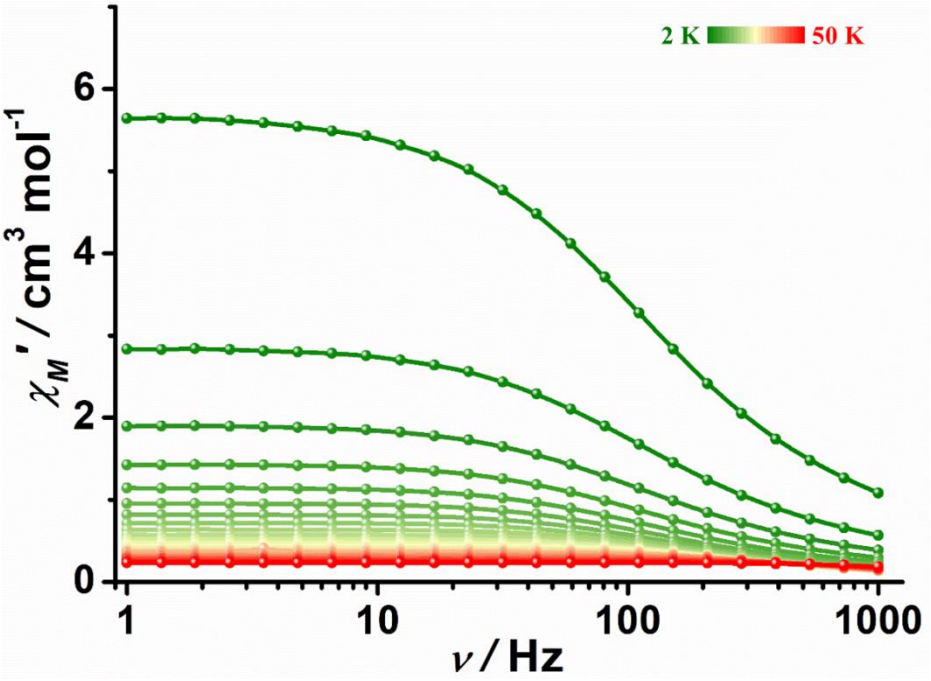

Figure S11. Frequency dependence of in-phase (χ_M') ac susceptibility for **1-Dy** under 0 Oe dc field; the solid lines are guides for the eye.

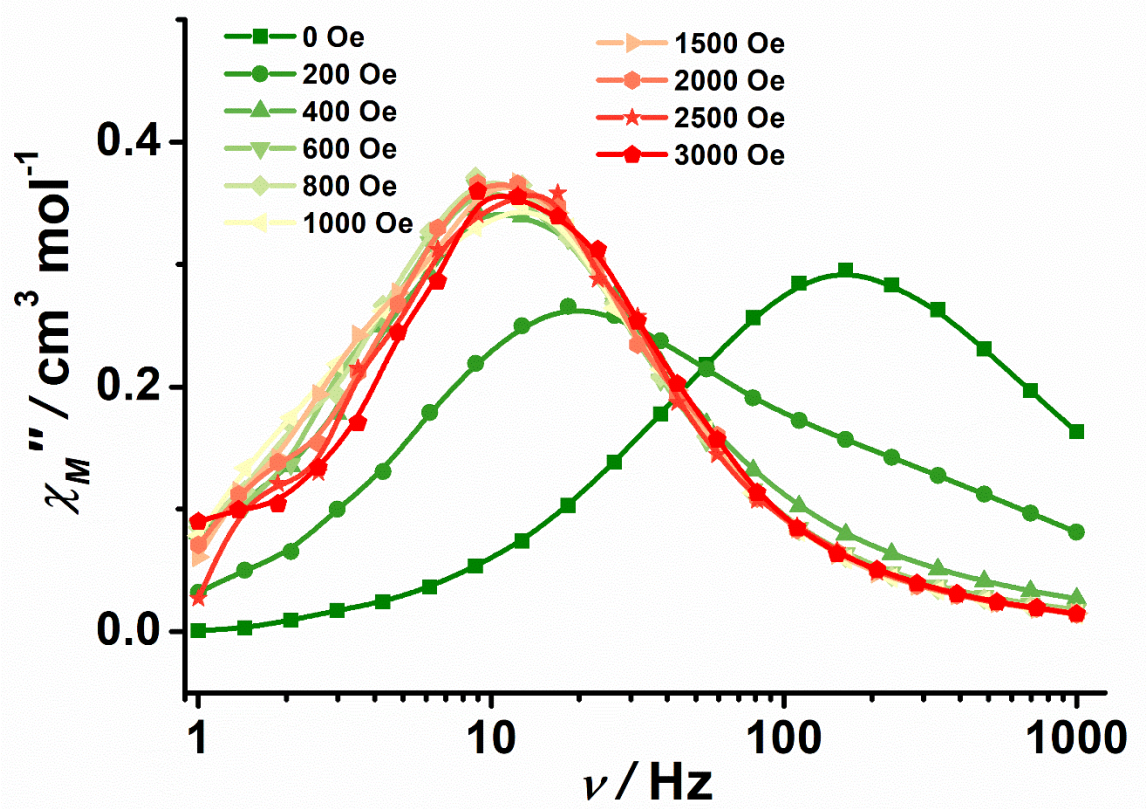

Figure S12. Field dependence of out-of-phase ac susceptibility (χ_M'') for **1-Dy** at 16 K. The lines are guides for the eye.

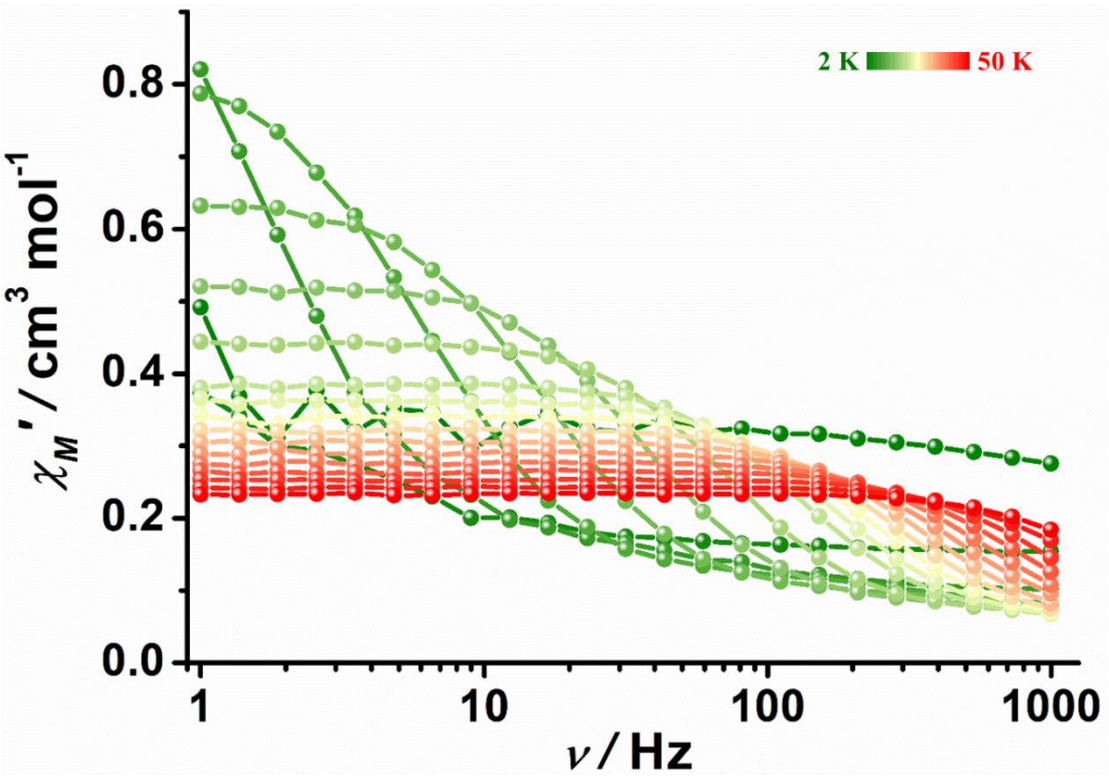

Figure S13. Frequency dependence of in-phase (χ_M') ac susceptibility for **1-Dy** under 2 kOe dc field; the solid lines are guides for the eye.

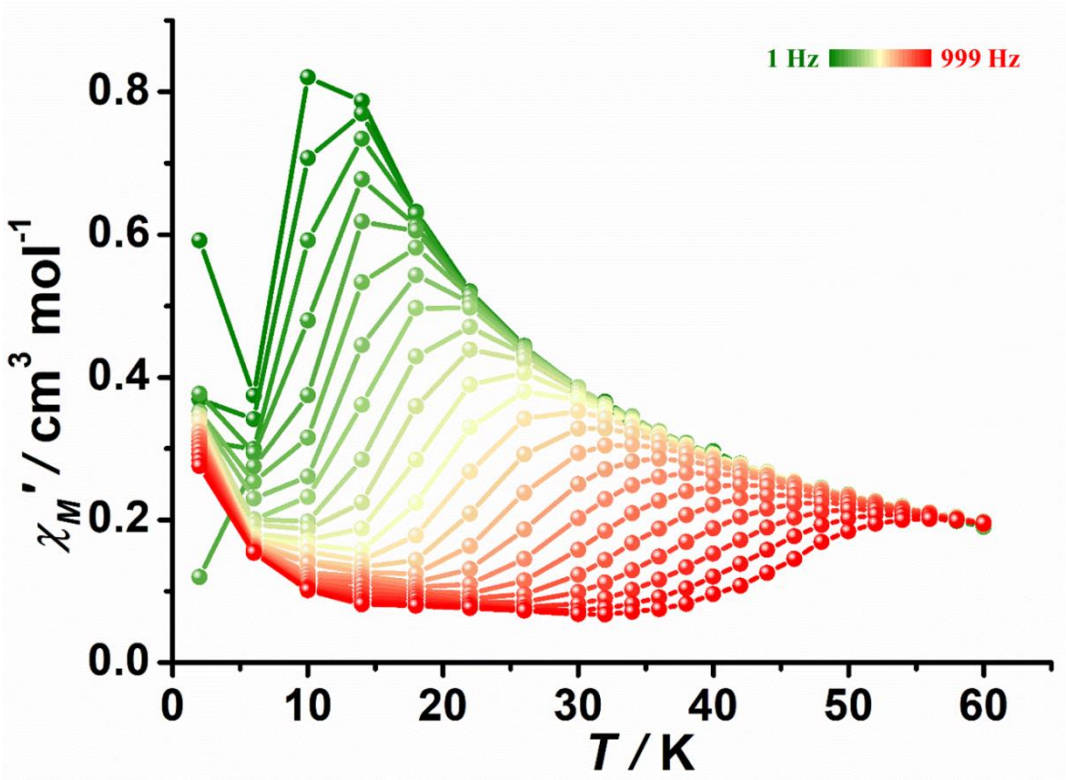

Figure S14. Temperature dependence of in-phase (χ_M') ac susceptibility for **1-Dy** under 2 kOe dc field; the solid lines are guides for the eye.

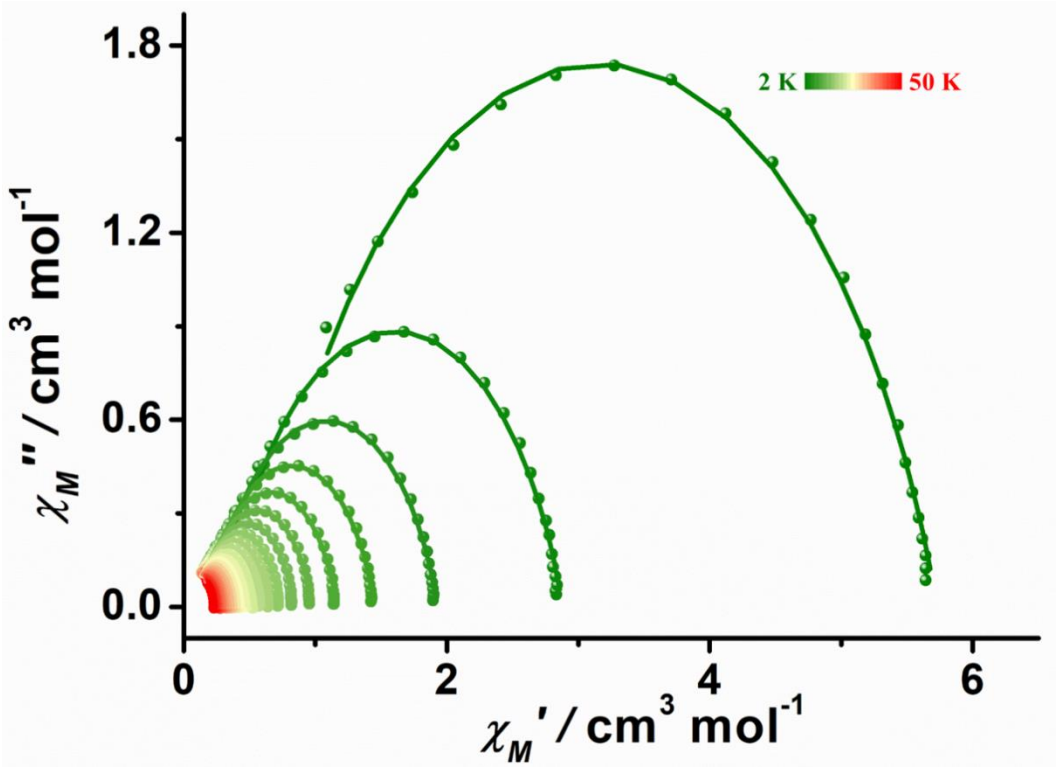

Figure S15. Cole-Cole plot of **1-Dy** under 0 Oe field, the solid lines correspond to the best fit to Debye's law.

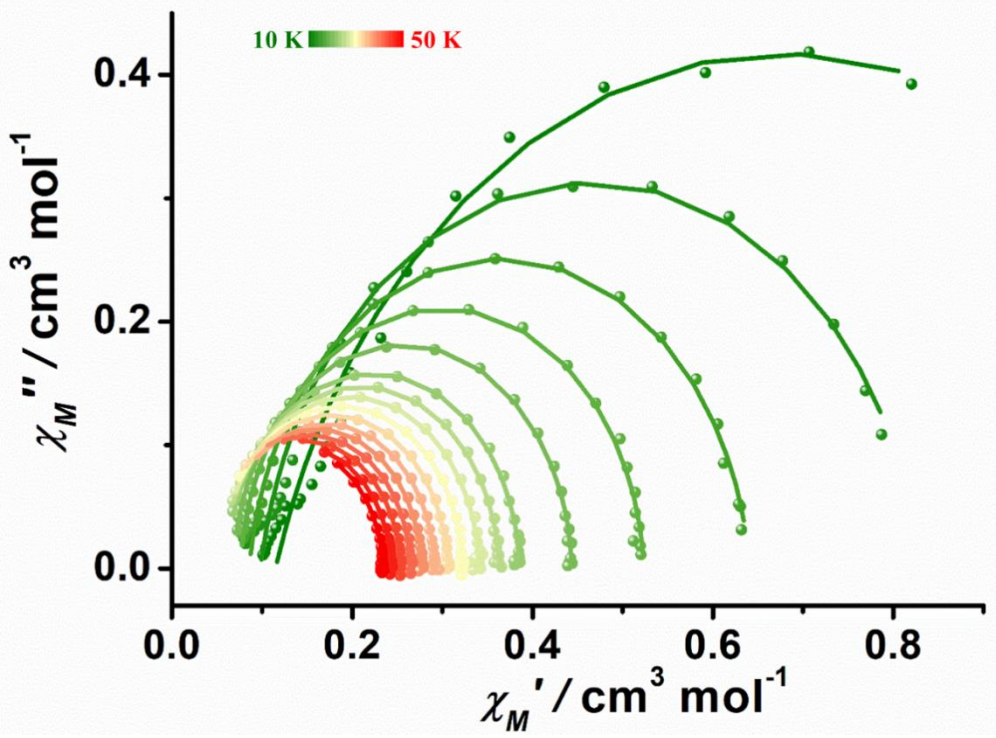

Figure S16. Cole-Cole plot of **1-Dy** under 2 kOe dc field, the solid lines correspond to the best fit to Debye's law.

Table S4. The parameters obtained by fitting the Cole-Cole plot under 0 Oe dc field for **1-Dy**.

T/K	χ_S	χ_T	τ	a
2	0.58917	5.72996	0.0013	0.24154
4	0.33313	2.88019	0.00128	0.22672
6	0.23713	1.92767	0.00125	0.21596
8	0.18652	1.44918	0.0012	0.20496
10	0.15621	1.15953	0.00114	0.1916
12	0.13623	0.96837	0.00107	0.17998
14	0.12125	0.82961	9.83189×10^{-4}	0.16836
16	0.11101	0.72638	9.0343×10^{-4}	0.15609
18	0.1031	0.6453	8.20876×10^{-4}	0.14409
20	0.09825	0.58092	7.42779×10^{-4}	0.12883
22	0.09234	0.52788	6.62321×10^{-4}	0.11729
24	0.08781	0.4843	5.89145×10^{-4}	0.10606
26	0.08453	0.44685	5.19407×10^{-4}	0.09243
28	0.0812	0.41575	4.56268×10^{-4}	0.08228
30	0.07861	0.38736	3.9882×10^{-4}	0.07077
32	0.06894	0.36762	3.43738×10^{-4}	0.09129
34	0.07126	0.3421	3.02123×10^{-4}	0.06137
36	0.0694	0.3235	2.64733×10^{-4}	0.05524
38	0.06795	0.3061	2.32074×10^{-4}	0.04729
40	0.06495	0.29126	2.02282×10^{-4}	0.04372
42	0.05968	0.27789	1.73704×10^{-4}	0.04546

44	0.05855	0.26504	1.52037×10^{-4}	0.03632
46	0.05725	0.25327	1.32471×10^{-4}	0.02158
48	0.05022	0.24406	1.08854×10^{-4}	0.03943
50	0.04651	0.23396	9.01211×10^{-5}	0.03357

Table S5. The parameters obtained by fitting the Cole-Cole plot under 2 kOe dc field for **1-Dy**.

T/K	χ_S	χ_T	τ	a
10	0.11506	1.2423	0.11026	0.18887
14	0.09818	0.83042	0.02551	0.10014
18	0.08597	0.64082	0.00959	0.06325
22	0.07631	0.52331	0.0043	0.03641
26	0.06847	0.44324	0.00216	0.01971
30	0.06073	0.38519	0.00119	0.01563
32	0.05628	0.36285	9.12491×10^{-4}	0.0225
34	0.05528	0.34023	7.04928×10^{-4}	0.01222
36	0.05245	0.32195	5.53814×10^{-4}	0.01256
38	0.04871	0.306	4.35573×10^{-4}	0.01953
40	0.05144	0.29071	3.50793×10^{-4}	0.01098
42	0.04452	0.27674	2.69252×10^{-4}	0.01484
44	0.04446	0.26416	2.12406×10^{-4}	0.00844
46	0.04149	0.25304	1.62792×10^{-4}	0.01009
48	0.03965	0.24289	1.22074×10^{-4}	0.01529
50	0.03072	0.23348	8.96287×10^{-5}	0.01438

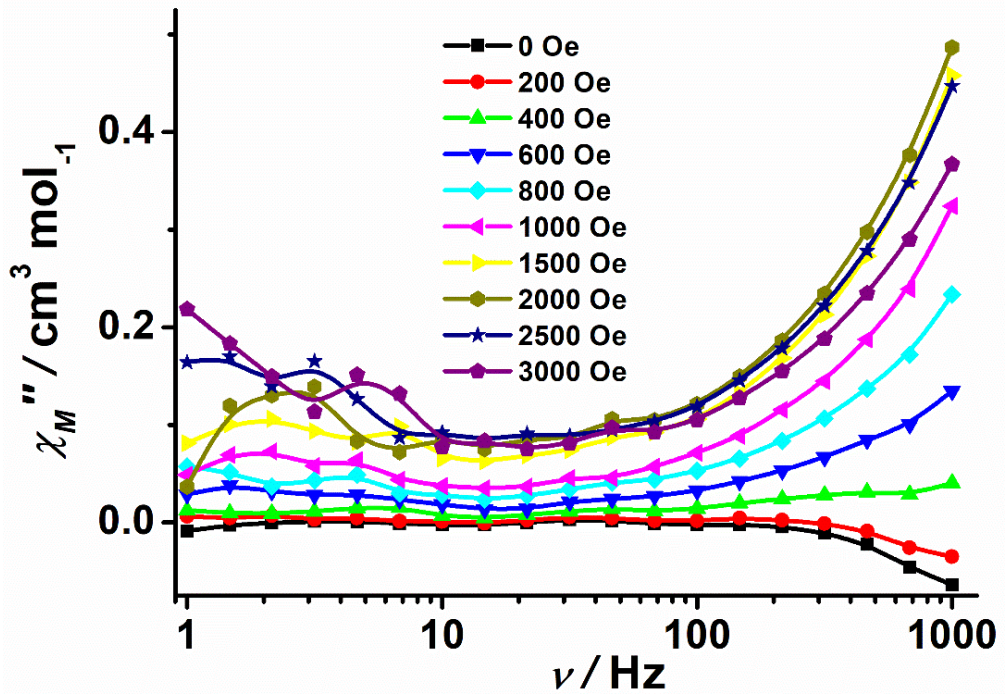

Figure S17. Frequency dependence of out-of-phase (χ_M") ac susceptibility at 2.0 K under the different applied fields from 0 to 3 kOe for **2-Tb**. The solid lines are for eye guide.

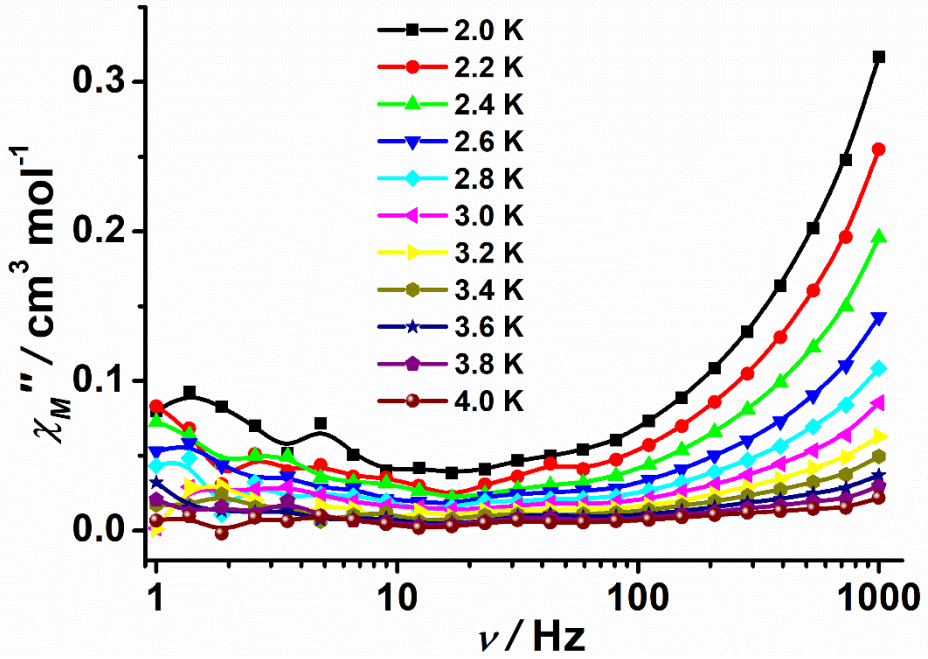

Figure S18. Frequency dependence of out-of-phase (χ_M'') ac susceptibility for **2-Tb** under 2 kOe dc field; the solid lines are guides for the eye.

Computational details

Multiconfigurational *ab initio* calculations, including spin-orbit coupling (SOC), were performed on selected systems. The geometries were taken from the crystallographic structures without further optimization. This type of calculation includes two steps:[S1] 1) a group of spin eigenstates, are obtained by the state-averaged (SA) CASSCF method;[S2] 2) the low-lying SOC states are obtained by diagonalizing the SOC matrix in the space spanned by the spin eigenstates from the first step. In the CASSCF step of **1-Dy**, the active space consisted of 9 electrons in 7 orbitals and all the spin eigenstates of 21 sextets were included. In the CASSCF step of **2-Tb**, the active space consisted of 8 electrons in 7 orbitals and 7 spin septet, 106 spin quintet, 283 spin triplet and 121 spin singlet states were included. The scalar relativistic effect is accounted via seond-order DKH transformation, i.e., DKH2 Hamiltonian. The second step was performed via the QDPT-SOC module[S3] with the SOC integrals from the SOMF method.[S4] The relativistic all-electron basis set SARC2-DKH-QZVP[S5] was used for Ln and DKH-def2-SV(P)[S6] was used for other atoms. All the *ab initio* calculations were performed with ORCA 5.0.3 code.[S7,S8] The SINGLE ANISO module[S9,S10] was used to obtain the g-tensors.

$$\tau_{\mathrm{QTM,i}}^{-1}(T) \propto \frac{\exp\left(-E_i/k_BT\right)}{Z}\tau_{\mathrm{QTM,i}}^{-1,\mathrm{eff}} \quad \text{(S1a)}$$

$$\tau_{\mathrm{QTM}}^{-1,\mathrm{eff}} = \frac{g_{\mathrm{XY,i}}^2}{2(g_{\mathrm{XY,i}}^2+g_{\mathrm{Z,i}}^2)^{\frac{1}{2}}} \quad \text{(S1b)}$$

$$Z = \sum_i \exp\left(-E_i/k_BT\right) \quad \text{(S1c)}$$

From eqn 1b, U_{eff} could be predicted based on TA-QTM in which both ground and excited KDs are included.[S1,S11] Thus the effect of thermal population should be included and the QTM rate of ith KD, i.e., $\tau_{\mathrm{QTM,i}}^{-1}(T)$ (eqn 3a), is estimated by the product of its Boltzman population and an effective QTM rate $\tau_{\mathrm{QTM,i}}^{-1,\mathrm{eff}}$ relying on the principal *g*-factors of this KD (eqn 3b). Finally U_{eff} is calculated as a weighted sum of the energies of different KDs (eqn 4a), with N being the normalization factor (eqn 4b).[S11]

$$U_{\mathrm{eff}}(T) = \sum_i \frac{\tau_{\mathrm{QTM,i}}^{-1,\mathrm{eff}}(T)}{N}E_i \quad \text{(S2a)}$$

$$N = \sum_i \tau_{\mathrm{QTM,i}}^{-1,\mathrm{eff}}(T) \quad \text{(S2b)}$$

Table S6. The *ab initio* energies and principal *g* factors of the lowest eight KD of **1-Dy**.

	g_X	g_Y	g_Z	E (cm^{-1})
KD_0	0.00155511	0.00232395	19.88209746	0.000
KD_1	0.14630447	0.15946332	16.88144348	356.036
KD_2	0.54119793	0.72257699	13.31956921	700.216
KD_3	4.44337040	5.54574244	9.47419910	906.931
KD_4	0.24239849	4.74862211	11.86708898	970.354
KD_5	0.92244315	5.30622232	12.61406485	1044.839
KD_6	0.85222760	2.33794495	13.45908468	1091.928
KD_7	1.55220717	3.80930890	14.81047243	1181.224

Table S7. The *ab initio* energies and principal g factors of the lowest eleven states of **1-Tb**[a].

	g_X	g_Y	g_Z	E (cm^{-1})
ID_0	0.000	0.000	17.80170461	0.000, 0.082
ID_1	0.000	0.000	14.77419854	129.415, 130.248
ID_2	0.000	0.000	11.53679135	309.460, 312.345
ID_3	0.000	0.000	8.30644994	510.934, 575.524
ID_4	0.000	0.000	5.12715641	779.316, 820.302
ID_5	0.000	0.000	2.33640291	1012.540, 1041.512
13th				1128.1927

[a] the lowest twelve states can be grouped into six quasi-degenerate doublets, termed as Ising doublet (ID).

References

S1 X.-X. Wu, J.-F. Li and B. Yin. The interpretation and prediction of lanthanide single-ion magnet from ab initio electronic structure calculation: The capability and limit, *Dalton Trans.*, 2022, **51**, 14793−14816.

S2 B. O. Roos, P. R. Taylor and P. E. M. Siegbahn, A COMPLETE ACTIVE SPACE SCF METHOD (CASSCF) USING A DENSITY MATRIX FORMULATED SUPER-CI APPROACH, *Chem. Phys.*, 1980, **48**, 157−173.

S3 D. Ganyushin and F. Neese, First-principles calculations of zero-field splitting parameters. *J. Chem. Phys.*, 2006, **125**, 024103.

S4 F. Neese, Efficient and accurate approximations to the molecular spin-orbit coupling operator and their use in molecular g-tensor calculations, *J. Chem. Phys.*, 2005, **122**, 034107.

S5 D. Aravena, F. Neese and D. A. Pantazis, Improved Segmented All-Electron Relativistically Contracted Basis Sets for the Lanthanides, *J. Chem. Theory Comput.*, 2016, **12**, 1148–1156.

S6 F. Weigend and R. Ahlrichs, Balanced basis sets of split valence, triple zeta valence and quadruple zeta valence quality for H to Rn: Design and assessment of accuracy, *Phys. Chem. Chem. Phys.*, 2005, **7**, 3297–3305.

S7 F. Neese, The ORCA program system, *WIREs Computational Molecular Science*, 2012, **2**, 73–78.

S8 F. Neese, Software update: The ORCA program system—Version 5.0, *WIREs Computational Molecular Science*, 2022, **12**, e1606.

S9 L. F. Chibotaru and L. Ungur, Ab initio calculation of anisotropic magnetic properties of complexes. I. Unique definition of pseudospin Hamiltonians and their derivation, *J. Chem. Phys.*, 2012, **137**, 064112.

S10 L. F. Chibotaru, *AB INITIO* METHODOLOGY FOR PSEUDOSPIN HAMILTONIANS OF ANISOTROPIC MAGNETIC COMPLEXES, *Advances in Chemical Physics*, Wiley VCH, Weinheim, 2013, **153**, 397–519.

S11 B. Yin and C.-C. Li, A method to predict both the relaxation time of quantum tunneling of magnetization and the effective barrier of magnetic reversal for a Kramers single-ion magnet, *Phys. Chem. Chem. Phys.*, 2020, 22, 9923– 9933.